Green Synthesis and Applications of Nano CeO₂/rGO Solar Active Photocatalyst for the Degradation of Basic Auramine-O Dye

A. Loganathan[1,2], A. Sivakumar[3], B. Murugesan[1,4] and P. Sivakumar[2,*,iD]

[1]Research and Development Centre, Bharathiar University, Coimbatore-641046, India
[2]Department of Chemistry, Arignar Anna Govt. Arts & Science College, Namakkal-637002, India
[3]Chemical Division, T.N.E.B. Limited, Mettur Dam-636406, India
[4]Department of Chemistry, K.S.R. Institute for Engineering and Technology, Tiruchengode-637215, India

*Corresponding author: E-mail: shivagobi@yahoo.com

In present study, the preparation of solar active photocatalyst and its application for the detoxification and degradation of dye molecules in aqueous medium is demonstrated. The reduced graphene oxide (rGO) is prepared from graphene oxide (GO) using *Carica papaya* leaf extract. Nanosize CeO₂ was coated over the rGO surface to make a nanocomposite photocatalyst. Prepared composite catalyst was characterized using SEM, HRTEM, XRD, EDX, FTIR, FT-Raman and UV-DRS techniques. The prepared composite catalyst was used for the degradation of auramine-O dye in its aqueous solution using UV and solar irradiations. The degradation kinetics is also evaluated using Langmuir-Hinshelwood kinetic model. The kinetic curves are analyzed using basic algorithm. A deviation from the experimental values and the reaction order is enumerated.

Keywords: CeO₂/rGO, *Carica papaya*, Photocatalytic degradation, Fractional order, Auramine-O dye.

INTRODUCTION

Over the decades, industrial sprawl and accumulation of population along river basins has created a huge amount of water pollution. Among the pollutants, dyeing industrial wastewater is a major concern, due to its toxicity, carcinogenic and deep coloring nature. The dye bearing wastewater creates huge environmental implications that directly affect the aquatic organisms and human beings [1,2]. Various physical, chemical and biological treatment technologies are reported for the removal of pollutants from the dye bearing wastewater. Some of them are adsorptive removal of dyes using high surface area adsorbents such as microporous [3] and activated spherical carbon spheres [4], chemical induced coagulation and flocculation by polymers [5], membrane separation like ultra- and nano-filtration [6,7] and advanced oxidation [8] technologies using atmospheric oxygen and biomes [9]. The applicability of the present technology is limited due to poor economic viability, poor selectivity towards dispersed dye, tedious optimization, longer adaptation period [10], massive sludge formation and

high energy input [11]. Using semiconductor photocatalysts, the detoxification and degradation can be achieved instantaneously with harmless end products.

TiO₂ [12], ZnO [13], ZnS [14], SnO₂ [15] and WO₃ [16] are some of the photocatalysts developed in recent times, extensively applied for photocatalytic dye degradation and organic compounds. Combined catalysts like SnO₂ co-doped with TiO₂ [17] and SnO₂ co-doped ZnO [18] are used as UV active photocatalysts for dye degradations. These semiconductor and chalcogenide catalysts have played eminent role in degrading the organic dyes with the help of UV light. Moreover, nano-architected carbon materials such as CNT along with semiconductor catalyst show a spectacular performance in photocatalysis. Recent investigations of CNT's superior electrochemical behaviour are promptly employed in super-capacitor electrodes as well as a hybrid material in energy storage appliances [19,20].

An allotropic, monolayered, one atom thick sp² hybridized carbon with a two-dimensional honeycomb matrix is known as graphene. Synthesis of graphene has opened up a spectrum of applications like lithium batteries [21,22], super-capacitors

[23], gas storage applications [24], advanced photovoltaic and optoelectronics [25,26]. The graphene functionalized with bio-molecules has found great applications in medical imaging through labeling and targeted delivery [27,28]. Graphene assisted structural hybrid of 1D, 2D and 3D macroscopic architectures [29,30] show pronounced synergistic effects by ion diffusion and charge transfer properties during electron transfer reactions. The exceptional conductivity is shown by graphene is due to its low resistance [31]. Graphene also has high specific surface area [32] due to its high surface-to-thickness ratio. The methodology employed for the preparation of graphene plays a major role in determining the morphology of graphene layers [33].

The nature of GO is highly distinguished from graphite because of the increased inter-layer spacing due to the oxygen functionalities [34,35] created between the layers. This oxygen insertion resulted in exfoliation of the oxidized graphene sheets into individual GO flakes in large quantities [34,36]. Further-more, the charge transfer is cut off in GO due to the strong locali-zation of the oxygen functionalities [37]. The reduction of GO gives rGO and it has graphene like structure with high electrical conductivity.

A UV light active semiconductor photocatalyst can be effec-tively modified into a visible light active catalyst by combining it with graphene based nano-carbon materials [38,39]. In latest study [39], we have prepared CeO$_2$ doped rGO by green syn-thesis to utilize the visible light for photocatalytic degradation of organic molecules. Sunlight is chosen as visible light source as it provides the renewable energy with wide spectrum of visible and UV ranged light. In this article, we have reported the synthesis, characterization and photocatalytic application of the semiconductor nano-CeO$_2$ doped rGO. It includes the con-version of graphite to graphene oxide using modified Hummer′s method followed by green reduction using *Carica papaya* leaf extract and doping with transition metal oxide. Moreover the selective catalyst was used for the treatment of dye effluent; the impact of pH and the concentration on degradation effi-ciencies were also investigated. The photodegradation studies were performed under UV and solar lights.

EXPERIMENTAL

Conc. H$_2$SO$_4$ and HCl, KMnO$_4$, C$_2$H$_5$OH (99.9 %), Ce(NO$_3$)$_3$·6H$_2$O, glycerol and NaOH were of analytical grade purchased and used as such. Basic auramine-O dye, (m.w. 304, m.f.: C$_{17}$H$_{22}$N$_3$Cl), C.I No. 41000, with an absorption maxima at 434 nm and graphite powder (Alpha Chemika, India) were used. Double distilled water was used for dilution and washing purposes.

Photocatalytic study: Photocatalytic degradation study of auramine-O is carried out using the prepared CeO$_2$/rGO catalyst in UV and direct solar-light irradiations separately in the specified rector setup [39]. The removal percentage of dye by photocatalysis was measured after completion of adsorption processes in dark. Based on the optimization studies, required quantity of catalyst was added in a selected concentration of dye solution and kept overnight to attain the adsorption equili-brium. Then the samples were irradiated with the selected light source for a specified period of time, separated from catalyst

by centrifugation at 5000 rpm for 5 min. The residual concen-tration of dye solution is analyzed by measuring the absorbance at the λ$_{max}$ of the respective solution. Double beam UV-visible spectrophotometer is employed for the absorbance measure-ments. The effect of pH on photodegradation is carried out by adjusting the pH of the dye solution using dilute HCl and NaOH. The quantum of dyes degraded by photocatalysis is measured by deducting the individual components of photolysis and adsorption. Exactly 5 g of 100 % auramine-O dye per liter was prepared as a stock solution using double-distilled water. Aliquots lower concentrations of auramine-O dye were prepared by diluting the stock solution.

UV photoreactor setup: Photocatalytic degradation studies was carried out using high-pressure mercury vapour lamp (160 W, 210-240 V) Philips, Indian make [Philips UVB Narrowband FS72 100W/01/UVB 19.5W/LAMP 126v/MODEL RDC (R17d)] as a central UV Lamp (λ = 365 nm) in a 12 reaction cells annular photo reactor (APR). The dye and the photocatalyst in pyrex tube reaction cells of capacity 150 mL are continuously stirred with magnetic stirrer during UV light irradiation.

Solar photoreactor assembly: Photodegradation by solar irradiation was carried by solar photoreactor assembly manu-factured using pyrex glass cooling jacketed beaker with magnetic stirrer. The experimental dye solution of a known dosage of photocatalyst is irradiated directly using sunlight without using any optical filters and devices. To minimize the evaporation loss of dye effluent and to maintain the reaction temperature, water flow is provided in the outer jacket. The marginal volume loss was made up to the mark by adding distilled water. The photo-catalytic dye degradation process by solar irradiation was carried out on clear sunny days between 11 a.m. to 3 p.m. only.

Synthesis of rGO

Conversion of graphite to GO: The first step in the prep-aration of rGO was the synthesis of GO from graphite using the modified Hummer′s method. In this method, 1 g of graphite was added to 23 mL of conc. H$_2$SO$_4$ in a round bottom flask. The content is cooled below 5 °C using ice with constant stirring. Along with this 3 g of powdered KMnO$_4$ is slowly added with constant stirring while the temperature of the flask is constantly maintained at 5 °C. After 1 h, the contents are allowed to attain room temperature naturally with constant stirring for 2 h contin-uously. With this solution, another 46 mL of double distilled water is added and the contents are heated to 95 °C for 30 min. The contents are then quenched with an addition of 140 mL of double distilled water. The GO formed is filtered and washed two times with 10 % HCl solution and finally with water.

Preparation of green extract: Matured *Carica papaya* leaves were collected from well grown papaya trees and thorou-ghly cleaned with water to remove unwanted surface contam-inants. The leaves are then cut in to pieces of 2 to 3 cm^2 size, grounded well and made into a paste with the help of a mortar and pestle and thoroughly mixed with small quantity of double distilled water. The contents were then filtered through Whatman No. 40 filter paper and the solid mass was discarded. The filtrate was used as reducing agent for the synthesis of rGO. In order to avoid the preservation practices every time, leaf extract of required quantity was freshly prepared.

Green synthesis of rGO: About 30 mg of GO was mixed with 50 mL of water and sonicated for 30 min. Followed by sonication, 30 mL of papaya leaf extract was added with constant stirring. The above mixture is heated to 95 ºC for about 12 h with a condenser on the top of round bottom flask to avoid the evaporative loss of volatiles. After 12 h of refluxing, black coloured rGO is filtered, washed well with double distilled water, dried in a hot air oven at 90 ºC and used for cerium oxide doping.

Synthesis of nano-CeO$_2$ doped rGO: Exactly 50, 100 and 250 mg of Ce(NO$_3$)$_3$·6H$_2$O was dissolved in 30, 60 and 150 mL of glycerol respectively with continuous stirring. Then each 500 mg of prepared rGO was taken in a round bottom flask and refluxed the the contents for 24 h in a N$_2$ atmosphere. Additional care was given during the process of this oxidation, the reaction was quenched with excess of water and centrifuged, washed with double distilled water and finally ethanol was used to remove leftover glycerol in the solution and then dried at 100 ºC overnight. The obtained CeO$_2$/rGOs were labeled as S1, S2 and S3, respectively.

Detection method: The morphological parameters of the samples were scanned by electron microscope (SEM) Hitachi S-4800 (NIT, Trichy, India) at an accelerating voltage of 5 kV and FEI Quanta 200 F SEM for field emission studies. For elemental analysis, energy dispersive X-ray (EDX) analyzer (Ametek) was engaged using non pre-treated samples at 30 kV with SDD Apollo X Detector. X-ray diffraction (XRD) patterns were recorded with a Rigaku Ultima III theta-theta gonio for powder and thin films (NIT, Trichy, India). Diffusion morphology images were observed with HRTEM (Jeol/JEM 2100-SAIF, STIC, Cochin, India). Functionalities of GO and various rGO were analyzed using FT-IR spectroscopy (Perkin Elmer-Spectrum RX I). D and G bands were elucidated with the help of FT-Raman analyzed in Bruker RFS 27. Diffuse reflectance spectrum (DRS) (DB-20S) was used to measure the absorption edge. Elico make BL-192 (UV-visible spectrophotometer) was used to measure the absorbance at the wavelenght of respective dye solutions to estimate the concentration.

RESULTS AND DISCUSSION

Characteristics of rGO and CeO$_2$ doped rGO: The efficiency of chemical treatment can be observed by analysis of FT-IR spectrum. FT-IR spectrum of rGO and CeO$_2$/rGO nanohybrids prepared by varying concentration of CeO$_2$, namely S1, S2 and S3 are shown in Fig. 1a. The peaks at 1096 and 1390 cm^{-1} in rGO are corresponding to C-O and epoxide functional group vibrations, respectively. The C-O stretching increased sharply in the hybrids due to the atmospheric CO$_2$ adsorption over ceria coated on rGO. Furthermore, absorption peak at 1680 cm^{-1} is due to the backbone vibrations of the remaining sp^2 hybridized carbon skeleton which was unaffected by oxidation [40]. A broad peak at 3450 cm^{-1} belongs to OH group [41]. CeO$_2$/rGO shows diminished peaks for the hydroxyl and C-O stretching frequencies. Moreover, the absorption peaks grow with the increasing concentrations of ceria at 1585 and 1735cm^{-1} due to the graphitized C=C and C=O functional groups. The epoxide stretching was relatively retarded by increasing the doped ceria concentration. It substantiated the replacement of ceria over the rGO surface. Further, FT-IR shows an incremental change with the increasing doped ceria concentration over rGO. Ce^{4+} forms coordination with carbonyls of rGO and observed the Ce-O stretching peak at 450 cm^{-1} [42]. Reported theoretical model concludes that the complete reduction of GO may be difficult [43]. But, FT-IR results indicate the rGO present in CeO$_2$/rGO has been reduced in a better way.

XRD analysis: XRD pattern of rGO and CeO$_2$/rGO samples S1, S2 and S3 prepared from GO by *Carica papaya* leaf extract as reducing agent are shown in Fig. 1b. In contrast to GO, rGO and CeO$_2$/rGO exhibited their reflection peak (002) at 25º and 26.2º respectively [44,45]. The *d*-spacing values of nearly 0.36 nm found uniformly in all the samples. The increased *d*-spacing represents the restacking in rGO as well as internal sandwiched CeO$_2$. The broadness of the peaks surpassingly sharpens from rGO to CeO$_2$/rGO samples imply the amorphous to crystalline transformation. The calculated particle size of doped CeO$_2$/rGO
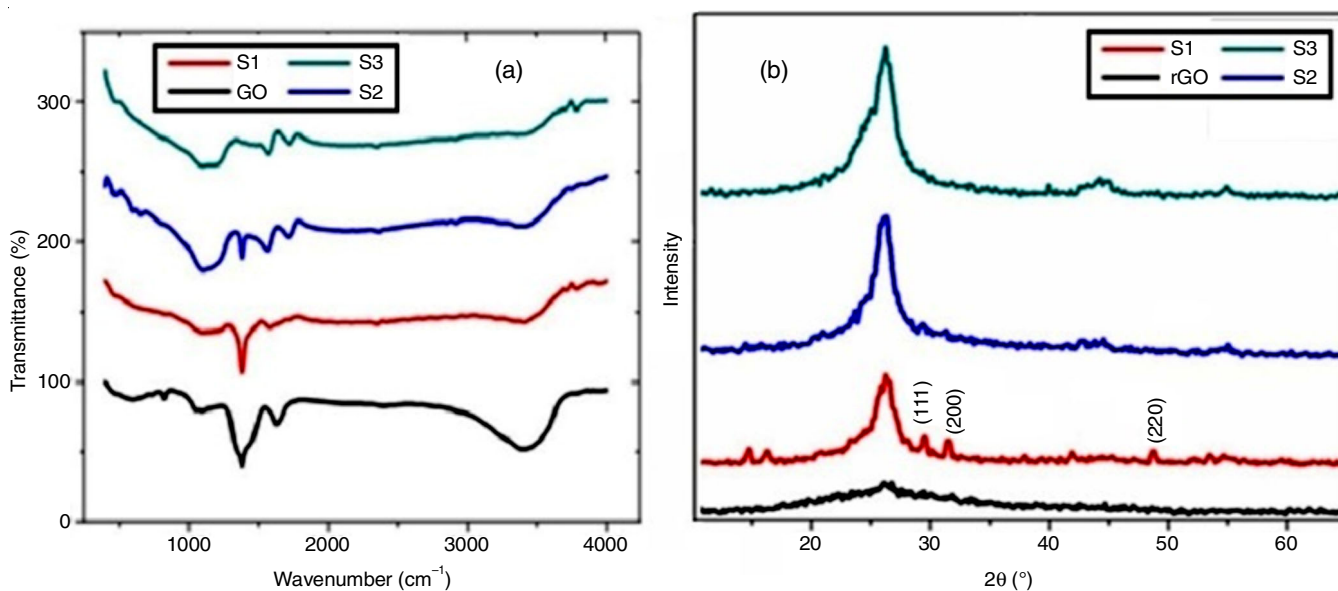

Fig. 1. (a) FT-IR spectrum and (b) XRD pattern of GO and CeO$_2$/rGO nanohybrids

is less (S2 sample), when compared to the other two samples (S1 and S3). The diffraction angle for the lattice plane are observed at 29.46º (111), 33.44º (200) and 48.68º (220), ensured from the ICDD number 01-075-9470 for face centered cubic ceria [46].

Raman analysis: Raman spectra for the green synthesized rGO and nanohybrid CeO$_2$/rGO (S2) are shown in Fig. 2. Defects and disorder of graphene based materials were broadly examined by Raman spectroscopy [47]. The D (1350 cm^{-1}) and G (1587 cm^{-1}) bands were the two characteristic first order scattering bands of graphene based materials. D bands are formed due to the impact by doping and covalent bonding with the lattice carbons and the G-band formed by the C-C vibrations of carbon with a sp^2 orbital structure. The D and G letters in Fig. 2 denotes the first order scattering bands. The intensity ratio I$_D$/I$_G$ for rGO is 1.10. It is manifested in terms of better reduction process cum increased disorder in graphene system and renewal of the structural perfection of sp^2 C in space. Heinz *et al.* [48] reported a blue shift in G band of graphene systems tend to lower Fermi energy and higher hole density. Analogous result is observed with 7 cm^{-1} blue shift in G band of CeO$_2$/rGO, will promote the electron transport performances of nanohybrid [49].
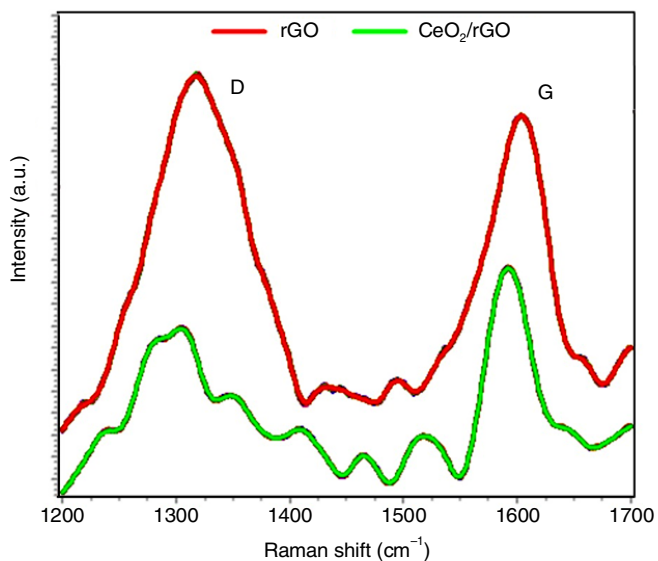

Fig. 2. Raman spectra of rGO and CeO$_2$/rGO nanohybrid (S2)

UV-visible-DRS analysis: The UV-visible DRS of S1, S2 and S3 are depicted in Fig. 3. The band gap energies (E$_g$) of these samples were calculated using the following energy equation, E$_g$ = 1239.8/λ, where 1239.8 correspond to multiplication factor of Plank's constant and velocity of light. The λ is the wavelength of light used. The band gap 3.08 (S1), 2.91 (S2) and 3.30 eV (S3) were calculated from the observed absorption limit of λ$_{max}$ at 402, 426 and 375 nm, respectively.

The obtained band gaps of CeO$_2$/rGO nanohybrid shows a reduction in band gap compared with CeO$_2$ (3.19 eV). These results are comparable with the results of bismuth oxide graphene nanocomposites [38]. The doped CeO$_2$/rGO sample S2, synthesized by green reduction process shows the BET surface area of 95 m^2/g. Among them S2 shows a narrower band gap and further used for photocatalytic studies.
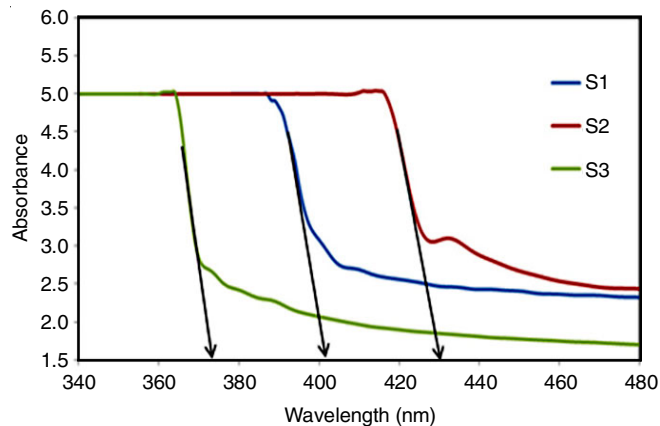

Fig. 3. UV-DRS spectrum of CeO$_2$/rGO nanohybrids absortion cutoff wavelengths

SEM analysis: The surface morphology and the particle size of synthesized GO and CeO$_2$/rGO doped samples S1, S2 and S3 were further examined using SEM analysis. SEM images at different magnifications of GO and CeO$_2$/rGO nanohybrid samples are shown in Fig. 4a-d, respectively. The image of GO describes the multi-layers of graphene separated spectacularly and it is in obvious agreement with the XRD *d*-space values of 002 lattice plane. All the GO sheets are regularly oriented and stacked parallel. The smooth surface morphology of GO also showed along with the EDAX of GO (inset Fig. 4a).

From the EDAX values, it was observed that considerable amount of oxygen content, substantiate the presence of C-O functionalities that ensures good oxidation in the first step of the preparation. Fig. 4b-d presents the morphological behaviours of nano-ceria doped rGO. On contrary with GO morphology, rGO nanosheets exhibit crumpled layer structure. All the rGO layers were coated with spherical nanosized CeO$_2$ over the surface and stacked parallel. A uniform distribution of CeO$_2$ nanoparticles was clearly visible on the peripheral of creased rGO nanosheets. The EDAX inset in Fig. 4d also validates the presence of cerium dopant quantitatively. Presence of minute quantities of non-metals and minerals of alkaline and alkaline earth metals could be due to the traces of reducing agent and the chemicals applied in the reaction process respectively.

HRTEM analysis: HRTEM images of CeO$_2$/rGO nano - hybrid catalyst (S2) have been illustrated in Fig. 5. It is evident from Fig.5 that the average grain size of these CeO$_2$ nanoparticles has been obtained as ~ 4-8 nm which is quite similar with the values obtained from XRD analysis. The images also substantiate the uniformly dispersed coating of cubic and quasi-spherical CeO$_2$ nanoparticles over the wrinkled rGO sheet. The diffraction pattern of CeO$_2$ particles also agrees with the XRD of the obtained cubic cerium(IV) oxide with the fluorite structure.

Photocatalytic degradation studies of auramine-O dye using CeO$_2$/rGO (S2): Photocatalytic degradation of auramine-O dye was studied with the help of CeO$_2$/rGO (S2) catalyst in UV and direct solar light irradiations and presented graphically in Fig. 6. It was necessary to omit the adsorption of dye on catalyst-composite surface for the calculation of net photocatalytic degradation. As seen from Fig. 6, the percentage of dye removal is gradually decreased from lower to higher
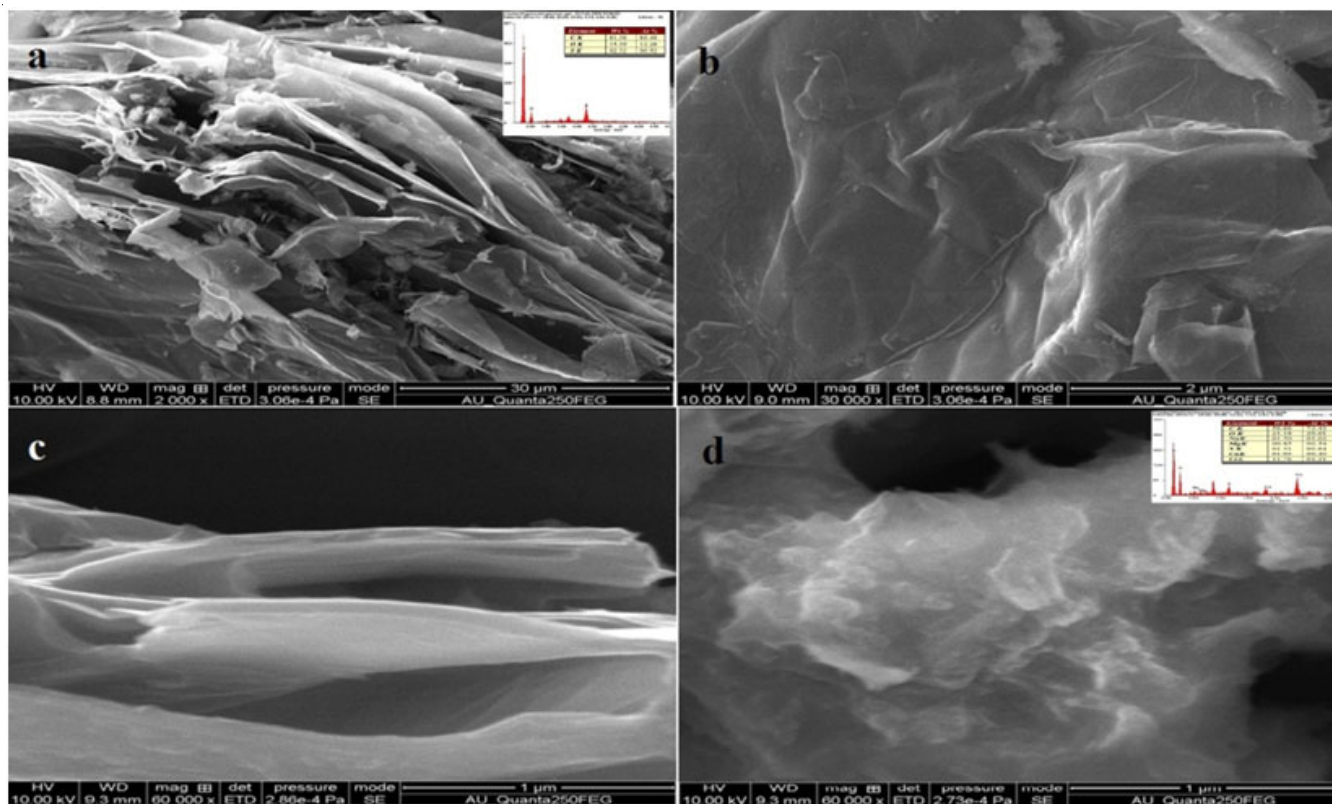
Fig. 4. (a) SEM image of GO and nanohybrid CeO$_2$-/rGO samples (b) S1, (c) S2 and (d) S3. The inset in 4(a) and 4(d) are the corresponding EDAX report of the materials
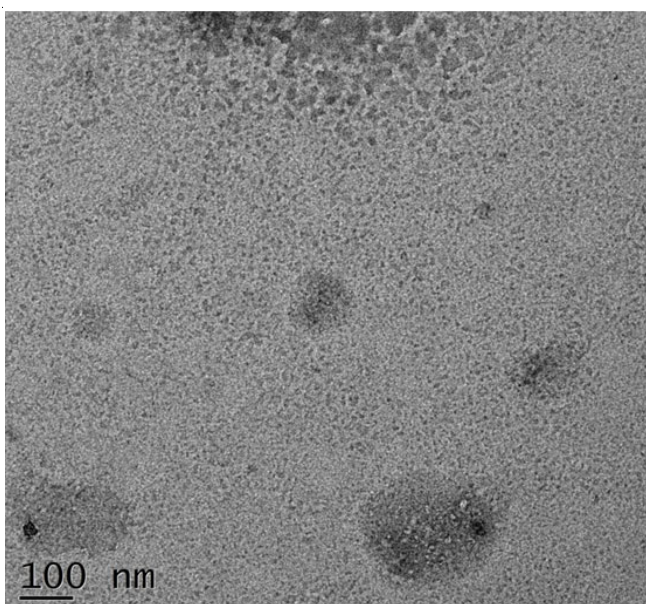

Fig. 5. HRTEM micrographs of CeO$_2$/rGO nanohybrid (S2)

dye concentrations for a specific catalyst dosage of 40 mg/L in both UV and solar irradiations.

The quantity dye adsorbed on rGO found a noticeable decrease on the doping with ceria due to the graphitic surface coated by the semiconductor catalyst, which eventually reduce the dye adsorption on carbon surface.

Effect of pH: The influence of solution pH on the adsorption of auramine-O dye onto the surface of rGO is studied at a pH range of 2.0 to 11.0 and presented in Fig. 7. There are

two factors to be considered while analyzing the mechanism of variation of adsorption with respect to pH. One is the changes occurring on the surface of catalyst and the ionization of dye molecules. On increasing the pH of solution, catalyst surface acquires a negative charge when the pH exceeds the pH point of zero charge (pzc) of the catalyst. When the pH exceeds 8, dye molecules experienced the similar charge repulsion by the sorbent surface. The rate of adsorption cum degradation decreases gradually on increasing the pH under solar light as well as UV light irradiations. Regarding the photodegradation of auramine-O dye process over CeO$_2$/rGO catalyst, at higher pH dye cations were attracted more towards catalyst, so augmented demand of holes (h$^+$) raised in OH$^\bullet$ radicals at higher pH [50].

Impact of catalyst load: It is essential to optimize the catalyst dosage for the efficient oxidative degradation of auramine-O dye by S2. For the optimization of catalytic dosage, catalyst dosage varied from 10 to 50 mg in 100 mL of auramine-O dye solution with an initial concentration of 150 mg/L. The solution kept at its natural pH and the photocatalytic degradation study was carried out for 100 min in UV and direct solar light irradiations separately. The photocatalytic dye degradation efficiency is given in Fig. 8.

Dye degradation efficiency is increased gradually with increasing catalytic dosage up to 40 mg of S2. Later, it shows a downward trend, due to the reduction in effective photoadsorption and screening effect. Further increase in catalyst dosage inverses the degradation efficiency. The optimum concentration catalyst dosage depend on many factors like the crystallinity, grain size, band gap, morphology, crystal defects, particle
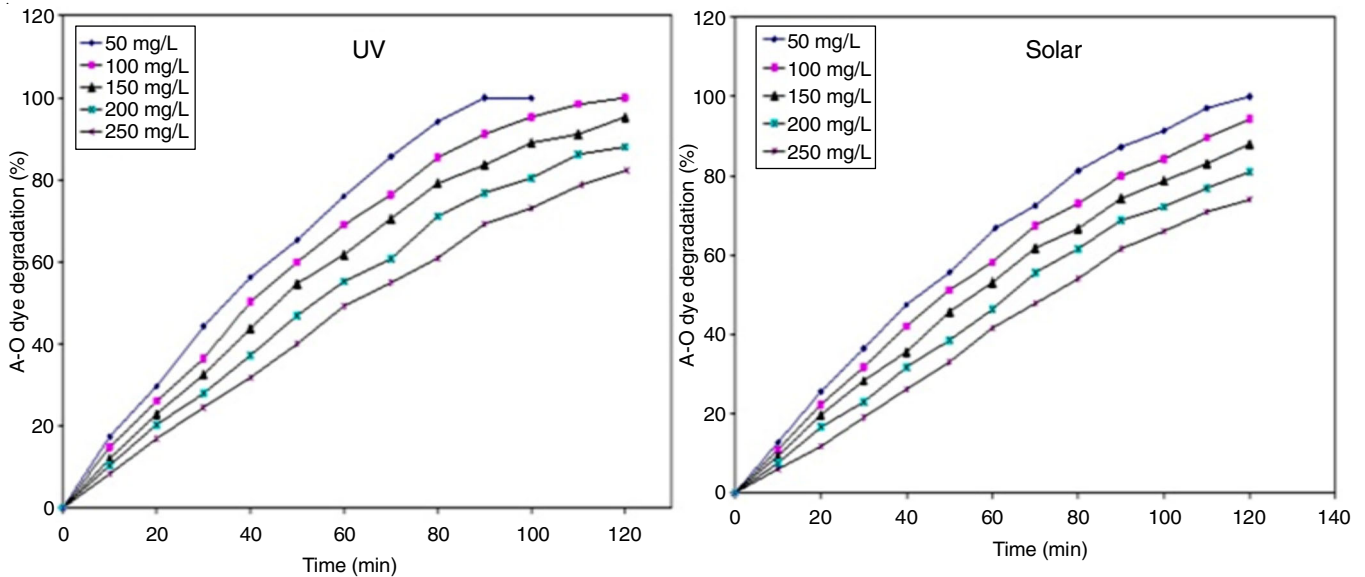
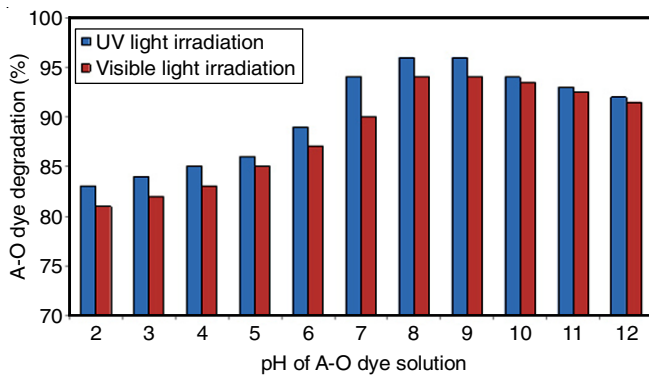Fig. 6. Photocatalytic degradation of various concentration of auramine-O dye under UV and solar lights

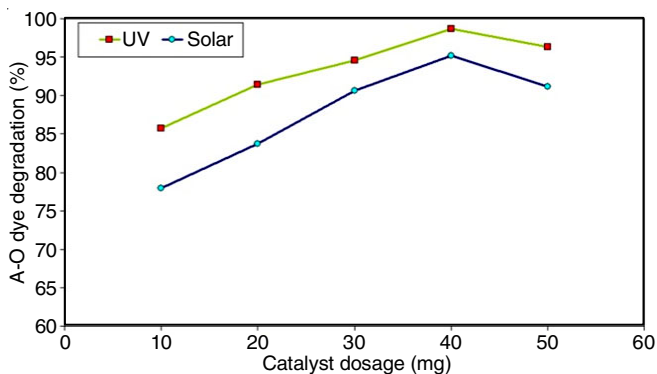Fig. 7. Effect of pH on photocatalytic degradation of auramine-O dye

Fig. 8. Effect of catalyst dosage on photocatalytic degradation of auramine-O dye

respect to time at various initial dye concentrations are shown in Fig. 9. The amount of auramine-O dye degraded was decreased from 100 % to 69 % and 91 to 66 % on increasing the initial auramine-O dye concentration from 50 to 250 mg/L under UV and solar light, respectively. The degradation efficiency was found to reverse with the addition of auramine-O dye concentration. Increasing the initial dye concentration influences the retardation of light penetration, which results in the least photon striking over the surface of catalyst. Previous reports [10,49] also supports the degradation trend on moving from lower to higher dye concentrations.
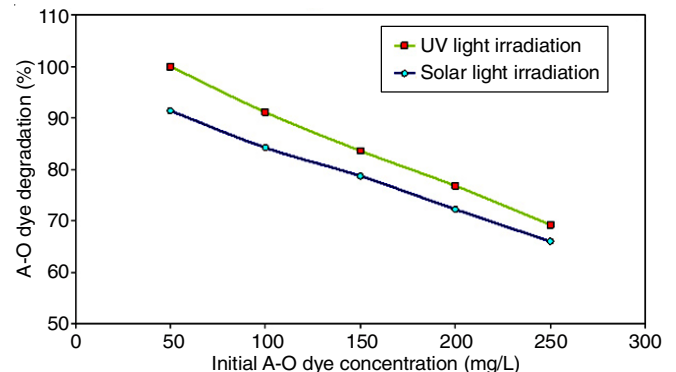

Fig. 9. Effect of dye concentration on photocatalytic degradation of auramine-O dye

Mechanism of photocatalytic degradation: A nanohybrid photocatalyst makes a relaxed photoelectron transfer. Electron emitted from the defective semiconductor CeO₂ surface was transferred to the highly conducting rGO surface [51]. Similarly, the rGO is capable of conducting electrons away from the semiconductor into the environment. The relocated electrons were used to reduce oxygen molecule in water by producing super oxide radical ions, thereby effectively delaying the recombination of e⁻-h⁺ pair in the semiconductor [52]. Retention of e⁻-h⁺ pairs ensures the availability of oxidizers and reducers.

size and the surface area [10]. Based on the above results, 40 mg of catalyst is fixed as the optimum loading for further photocatalytic studies.

Effect of initial dye concentration: The effect of initial concentration of auramine-O dye solution on photodegradation by CeO₂/rGO is studied by varying the initial dye concentration from 50 to 250 mg/L with a fixed volume of 100 mL and catalyst dosage of 40 mg under UV and solar irradiations separately.

The study is carried out for 100 min at the natural pH of the aqueous dye solution. The variation of dye degradation with

Holes in semiconductor oxidize the OH$^-$ ions to OH$^{\bullet}$ radicals. The resultant super oxide radical ion and OH$^{\bullet}$ radicals in aqueous medium were responsible for the degradation of dyes through redox reaction [10]. Overall mechanism of the photo-degradation and possible photochemical reaction involved are presented pictorially in Fig. 10.

Kinetics of photocatalytic degradation of auramine-O dye: Kinetics of heterogeneous system has a great importance during the large scale implementation photocatalysis at the industrial scale [53]. It is most suitable to evaluate the kinetics of photodegradation of auramine-O dye by photocatalyst CeO$_2$/rGO (S2) using the following kinetic model expressed by Langmuir-Hinshelwood equation:

$$\ln C_t = -k_{app} t + \ln C_o \qquad (1)$$

where, C_o and C_t is the initial concentration and concentration at time t (min) in the photocatalytic reaction and k_{app} ($k_r k_e$) is the pseudo-first order apparent rate constant (min^{-1}). The k_{app} was measured from the slope of the curve obtained by plotting time *versus* ln C_t as shown in Fig. 11a and 11b for UV and solar
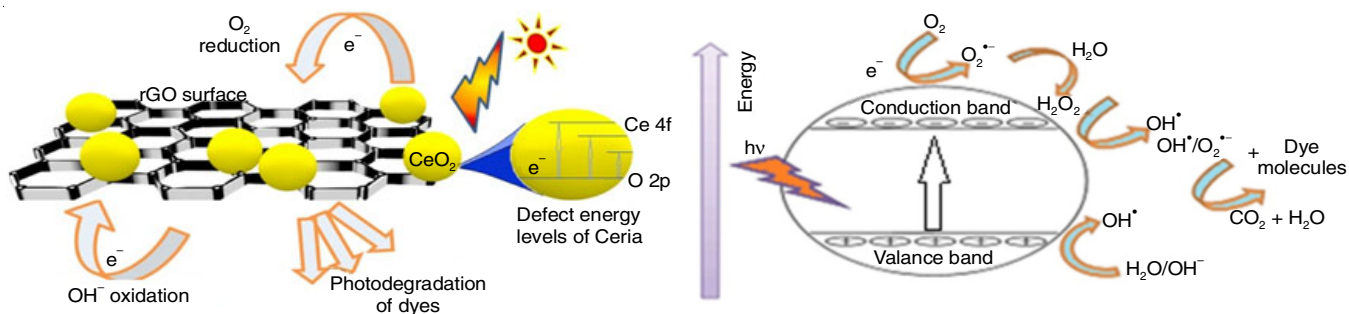

Fig. 10. Mechanism of photodegradation and its possible chemical reactions over CeO$_2$/rGO nanohybrid
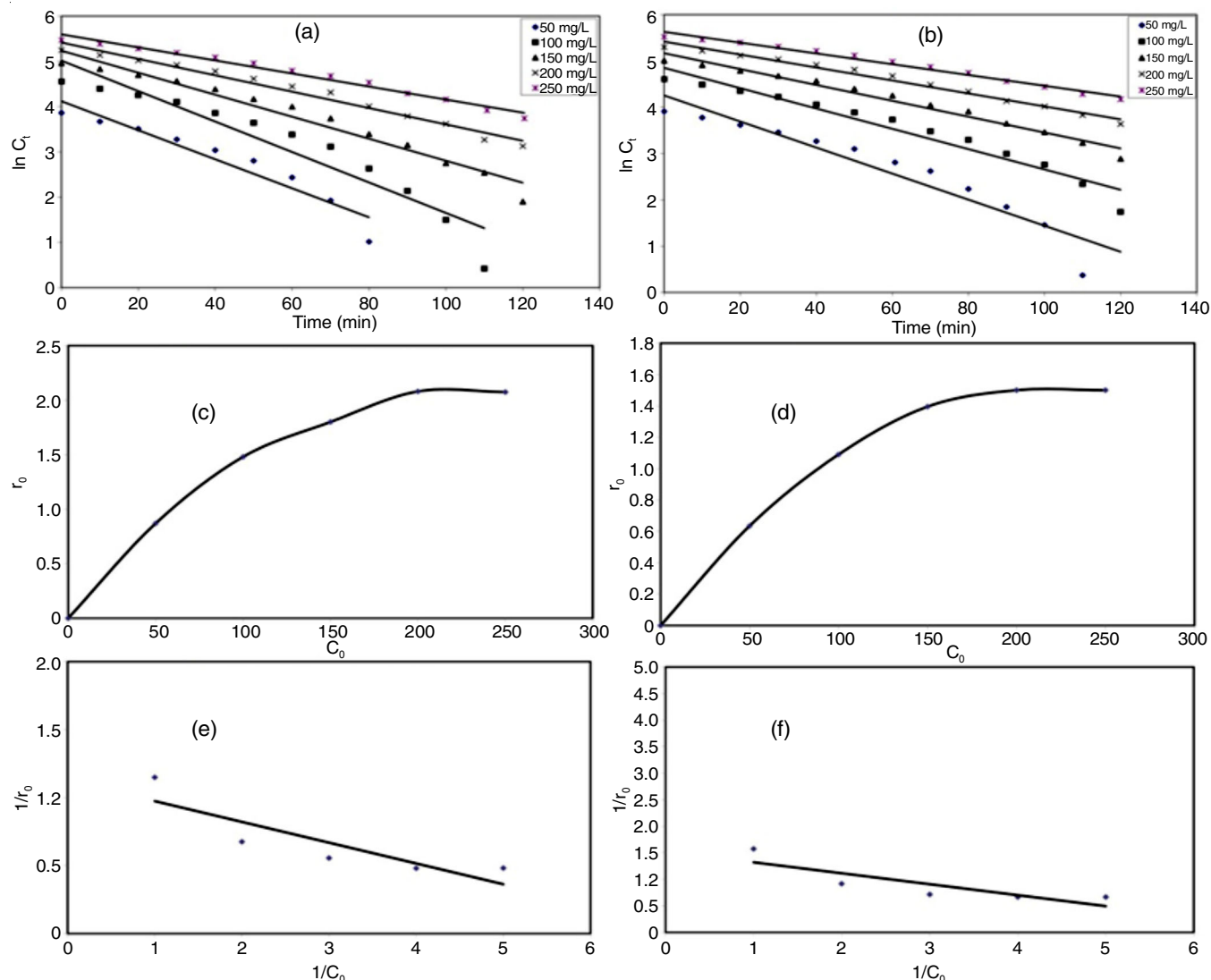

Fig. 11. First order plot for photodegradation of auramine-O dye (a) under UV and (b) under solar light, corresponding C$_o$ *vs.* r$_0$ -and 1/C$_o$ *vs.* 1/r$_o$ plots of (c) & (e) for UV and (d) & (f) for solar lights, respectively

irradiated dye degradation studies, respectively. The k_{app} and r^2 values for the plots are given in Table-1 for various initial auramine-O dye concentrations.

TABLE-1
PSEUDO-FIRST ORDER KINETIC RESULTS OF
AURAMINE-O DYE PHOTODEGRADATION BY S2

Initial dye conc. (mg/L)	Under UV light		Under solar light	
	k_{app}	r^2	k_{app}	r^2
50	0.0739	0.9154	0.0647	0.9101
100	0.0778	0.9038	0.0504	0.9481
150	0.0560	0.9612	0.0394	0.9756
200	0.0417	0.9770	0.0322	0.9838
250	0.0332	0.9809	0.0267	0.9841
Average	0.0565	0.9477	0.0427	0.9603

Table-1 shows a minimum deviation of r^2 value. It is obvious that the photocatalytic degradation of auramine-O dye by CeO₂/rGO (S2) follows pseudo-first order kinetics. First order kinetics of photodegradation too infers the gradual retardation in rate constant irrespective of light used for the photodegradation. This may be due to the fully engaged catalyst surface, which further delayed degradation.

Rearranging eqn. 1 gives,

$$\frac{1}{r_o} = \frac{1}{k_r} + \frac{1}{k_r k_e} C_o \tag{2}$$

where, k_r and k_e are the reaction rate constant and the equilibrium constant for the adsorption.

Plot of C_o versus r_o using eqn. 2 describes the linear relationship up to the initial dye concentration of 150 mg/L. Further increase in the initial concentrations will not show any improvement in the rate of degradation. This shows that the saturation of adsorption sites over the catalyst surface occurred as shown in Fig. 11c-d. Saturated type Langmuir kinetics [54] is suggested from the linear plot of $1/r_o$ versus $1/C_o$ as shown in Fig. 11e-f.

Heterogeneous catalytic photodegradation of organic pollutants like pentachlorophenol (PCP) and organic dyes using solid semiconductor photocatalysts suitably fit into the Langmuir-Hinshelwood (LH) kinetic model [55,56]. The following eqn. 3 is the most commonly used kinetic expression, which relates the rate of decrease of concentration with respect to time to its rate and equilibrium constants as

$$-\frac{dC}{dt} = \frac{k_r k_e C}{1 + k_e C} \tag{3}$$

where, C represents the concentration of dye solution degraded in terms of mg/L and at a given reaction temperature. k_r and k_e are the reaction rate constants (mg/L/min) and the equilibrium constant for the adsorption of dye molecules on the catalyst surface (L/mg). The product of k_r and K_e is generally termed as the apparent rate constant (k_{app}; min⁻¹) [57]. Substituting this in eqn 3, results as:

$$-\frac{dC}{dt} = \frac{k_{app} C}{1 + k_e C} \tag{4}$$

In the above equations, the factor $1+k_e C$ turns to unity or depends more on the $K_e C$ value, either $\ll 1$ or $\gg 1$ allows this equation to rearrange. It results in two possible routes,

classical first or zero order, when the concentration of dye solutions used were too low or high, respectively. First and zero order equations are presented in eqns. 5 and 6 respectively [58]:

$$-\frac{dC}{dt} = k_{app} C \tag{5}$$

and

$$-\frac{dC}{dt} = \frac{k_{app}}{k_e} = k_r \tag{6}$$

For a heterogeneous system [59], the following power rate equation for the reaction rate is commonly used to evaluate C using t and k_{app},

$$-\frac{dC}{dt} = k_{app}^* C^n \tag{7}$$

The power factor n varies from 0 to 1, as in eqns 6 and 7 at the two extremes. In case of n is greater than one, it may be of significance either in the non-uniformed distribution of radiation in the reactor or photo-corrosion, which typically occurs in catalysts such as ZnO [58,60]. This type of photo corrosion is restricted in sample S2 naturally due to the surface oxygen sharing in between carbon and cerium metal centers in CeO₂/rGO as evident from the FT-IR results. Eqn. 7 on integration within the limits of 0 and 1, make possible for the direct evaluation of the reactant concentration by the expression:

$$C = \left[C_o^{(1-n)} - (1-n) k_{app}^* t \right]^{1/(1-n)} \tag{8}$$

while using the power rate eqn 7, to calculate the order, it was found that it deviates from the ideal first order equations, although it is maintained between 0 and 1 with the increase of dye concentration. For the same initial concentration, eqn. 8 can only be practical to fit the curves [58].

Generally, the linear form of integrated first order equation was used [61], which gives a straight line fitting as shown in Fig. 11a-b. According to Lima et al. [62], the linearization of data was misrepresented in many adsorption related data analysis. The linearization is followed during the time where the computers and data analysis software were not available. In the linearized plot, there is a possibility of omitting many points that were not coincided with the straight line and it is applicable especially for lesser number of experimental data points. The analysis of more number of experimental data points using linear model may lead to an erroneous result [63]. The k_{app} and r^2 calculated for various initial dye concentrations are given in Table-1, which confirmed whether the photocatalytic degradation of dye by sample S2 follows pseudo-first order or second order kinetics.

We used eqn. 1 to fit in the experimental data by means of least square method, which leads to minimize the error in $\ln (C_o/C)$ function (ε_{ln}) only but not minimizing the error in C (ε_c) [55]. For this reason, eqn. 8 is fitted to minimize ε_c, the non-linear function by employing standard algorithms with the aid of "Microsoft Excel-Solve" application. By employing this mathematical application, the curve was fitted at the most possible way in order to minimize the error in concentration term (ε_c) by tuning the order of reaction and evaluated the same from eqn 8. The curve fitting method shows fractional order for the process of photodegradation of dyes using CeO₂/

TABLE-2
KINETIC PARAMETERS OF AURAMINE-O DYE PHOTODEGRADATION UNDER UV AND SOLAR IRRADIATIONS

Light used	Various initial concentration (mg/L) of auramine-O dye degradation														
	Sum of the $(C_t\text{-model } C_t)^2$					Order (n)					Reaction rate constant (k^*_{app})				
	50	100	150	200	250	50	100	150	200	250	50	100	150	200	250
UV	3.8	13.2	33.9	77.3	60.1	0.373	0.444	0.44	0.414	0.347	0.189	0.186	0.207	0.235	0.326
	17.9	87.6	290.0	530.5	756.1	0.647	0.643	0.735	0.776	0.797	0.074	0.078	0.056	0.042	0.033
	61.0	369.3	784.8	1087.3	1349.1	1.000	1.000	1.000	1.000	1.000	0.024	0.019	0.018	0.015	0.012
Solar	4.2	3.9	17.4	84.2	235.1	0.499	0.434	0.416	0.337	0.345	0.099	0.158	0.190	0.289	0.281
	15.9	90.8	227.8	521.5	1030.4	0.626	0.716	0.765	0.789	0.816	0.065	0.050	0.039	0.032	0.025
	82.7	287.7	517.8	909.2	1473.4	1.000	1.000	1.000	1.000	1.000	0.019	0.017	0.014	0.012	0.010

rGO. The results are in good agreement with the order of the reported photocatalytic degradation reaction of phenol using TiO_2 P25 particles [58].

Using this non-linear equation, we can calculate the "Model C_t" by applying the corresponding initial concentration (C_o) of auramine-O dye and at the time 't' min. For a particular C_o and 't', "Model C_t" values are totally depending on n and k^*_{app} (apparent rate constant for heterogeneous catalysis). Basic algorithm (Levenberg-Marquardt) helps to solve "Model C_t" to fix exactly with the experimental C_t values. Most possible fitting was enabled by changing the n and k^*_{app} suitably with the help of the "Excel-solve" tool, resulting in lowest deviation of $\Sigma(C_t - \text{Model } C_t)^2$. The experimental C_t values from the practical observations and the calculated $(C_t - \text{Model } C_t)^2$ values are presented in Table-2.

The curve plotted against C_t and t for the 50, 100, 150, 200 and 250 mg/L concentrations of auramine-O dye under UV as well as solar light and the most possible fittest curve also reproduced over the curve (figure not shown). Curve a was fitted by eqn. 8 and the resultant n and k^*_{app} was derived for the minimum error. Curve b is fitted with fixed k^*_{app} value, which is

directly taken from the experimental rate constant (k_{expt}). This k_{expt} values derived from the slopes of the linear equated (1) in first order plot of the corresponding concentrations and resultant n with its possible errors were derived. Curve c was plotted by fixing the n value as 0.99 (for 1st order) and curve fitted by synchronizing only k^*_{app}. Errors $\Sigma(C_t - \text{Model } C_t)^2$ for all the three type of plots were compared in Table-2. The data also revealed the best suited fractional order and the lowest deviation from the experimental C_t values in all concentrations under UV and solar irradiations.

The plot shown in Fig. 12 imparts the sum of the square deviations against the concentration of dye. This clearly depicted that the curve fitting option shows minimum deviation (ε_c – average error) and the best fit while using eqn 9, when compared with the other two methods (k_{expt} and n = 1) under all the concentrations of auramine-O dye. This will eventually put forward the fractional ordered Langmuir-Hinshelwood kinetics for the photodegradation of auramine-O dye under UV and solar light.

The fractional order varies from 0.37 to 0.44 and 0.34 to 0.50 for UV and solar light for the degradations of auramine-O dye by CeO_2/rGO (S2), respectively. This is obtained by curve
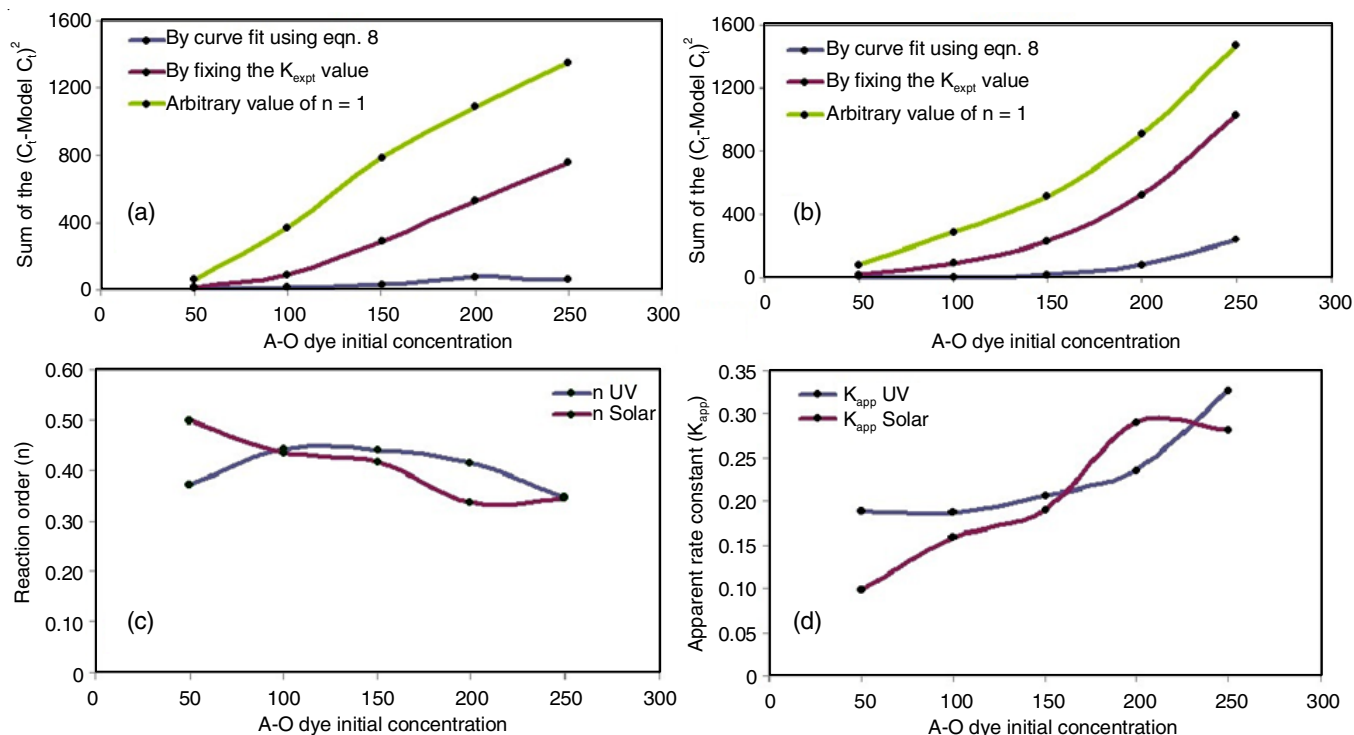

Fig. 12. Plots of sum of the square deviations under (a) UV and (b) solar lights; corresponding (c) order and (d) apparent rate constant observed by curve fit operation using eqn. 8

fitting eqn 8 as shown in Fig. 12c. This fractional order is greatly influenced by the by-products formed from the degradation of dye molecules during photocatalysis. This may again compete with the dye molecules during the photodegradation process. Naturally, further degradation of fragmented molecules may also consequence with the on-going primary degradation of the dye, resulting in variable functional adsorption processes over the photocatalyst. Hence, it makes this adsorption cum photodegradation process more complex.

According to chemical kinetics and dynamics by Steinfeld *et al.* [64], a fractional reaction order indicates that mechanism for the reaction is more complicated. The mechanism probably entails several elementary reactions. It is evident to analyze that the complexity of the photocatalytic process has resulted with the fractional order with respect to dye molecule degradation. The degraded products of basic methylene blue dye also ensures plenty of degraded products existed during the photocatalysis from the research investigation carried out by Ahmad *et al.* [65]. The rate constant (k^*_{app}) of reaction varies from 0.19 to 0.33 and 0.10 to 0.29 for the UV and solar light driven photocatalytic degradation of auramine-O dye obtained by curve fitting eqn 8 as shown in Fig.12d.

Conclusion

This work examines a green approach that has been successfully applied for the synthesis of nanohybrid photocatalyst. *Carica papaya* leaf extract was used as a green reducing agent for the conversion of GO to rGO. CeO₂/rGO nanohybrid is successfully made by chemical co-doping of nano CeO₂ over the conductive rGO. Among three samples prepared S1, S2 and S3, sample S2 showed an observable change in its optical properties. The composite catalyst CeO₂/rGO nanohybrid has the cubic ceria particles of ~ 4-8 nm size and lowest band gap energy of 2.91 eV with good electron transport performance. Photocatalytic reaction kinetics for auramine-O dye degradation under UV and solar light with a catalyst dosage of 40 mg/100 mL obeys Langmuir-Hinshelwood pseudo-first order kinetics. However, curve fitting substantiated that the photocatalytic process precedes though fractional order with respect to the initial dye concentration of dye. The impact of pH, dye concentration and catalyst dosage on dye degradation are conferred and the photocatalytic degradation mechanism is also successfully demonstrated.

CONFLICT OF INTEREST

The authors declare that there is no conflict of interests regarding the publication of this article.

REFERENCES

1. D.L. Lewis, W. Garrison, K.E. Wommack, A. Whittemore, P. Steudler and J. Melillo, *Nature*, **401**, 898 (1999);
   https://doi.org/10.1038/44801

2. S.S. Epstein, S. Joshi, J. Andrea, N. Mantel, E. Sawicki, T. Stanley and E.C. Tabor, *Nature*, **212**, 1305 (1966);
   https://doi.org/10.1038/2121305a0

3. P.N. Palanisamy and P. Sivakumar, *Desalination*, **249**, 388 (2009);
   https://doi.org/10.1016/j.desal.2009.09.006

4. K.C. Bedin, A.C. Martins, A.L. Cazetta, O. Pezoti and V.C. Almeida, *Chem. Eng. J.*, **286**, 476 (2016);
   https://doi.org/10.1016/j.cej.2015.10.099

5. A.K. Verma, R.R. Dash and P. Bhunia, *J. Environ. Manage.*, **93**, 154 (2012);
   https://doi.org/10.1016/j.jenvman.2011.09.012

6. E. Alventosa-deLara, S. Barredo-Damas, M.I. Alcaina-Miranda and M.I. Iborra-Clar, *J. Hazard. Mater.*, **209**, 492 (2012);
   https://doi.org/10.1016/j.jhazmat.2012.01.065

7. M. Riera-Torres, C. Gutiérrez-Bouzán and M. Crespi, *Desalination*, **252**, 53 (2010);
   https://doi.org/10.1016/j.desal.2009.11.002

8. N. Azbar, T. Yonar and K. Kestioglu, *Chemosphere*, **55**, 35 (2004);
   https://doi.org/10.1016/j.chemosphere.2003.10.046

9. P. Kaushik and A. Malik, *J. Hazard. Mater.*, **185**, 837 (2011);
   https://doi.org/10.1016/j.jhazmat.2010.09.096

10. A. Sivakumar, B. Murugesan, A. Loganathan and P. Sivakumar, *J. Taiwan Inst. Chem. Eng.*, **45**, 2300 (2014);
    https://doi.org/10.1016/j.jtice.2014.07.003

11. T. Bechtold, E. Burtscher and A. Turcanu, *J. Chem. Technol. Biotechnol.*, **76**, 303 (2001);
    https://doi.org/10.1002/jctb.383

12. C.H. Kwon, H. Shin, J.H. Kim, W.S. Choi and K.H. Yoon, *Mater. Chem. Phys.*, **86**, 78 (2004);
    https://doi.org/10.1016/j.matchemphys.2004.02.024

13. M. Quintana, E. Ricra, J. Rodríguez and W. Estrada, *Catal. Today*, **76**, 141 (2002);
    https://doi.org/10.1016/S0920-5861(02)00214-6

14. J.S. Hu, L.L. Ren, Y.G. Guo, H.P. Liang, A.M. Cao, L.J. Wan and C.L. Bai, *Angew. Chem. Int. Ed. Engl.*, **44**, 1269 (2005);
    https://doi.org/10.1002/anie.200462057

15. H. Wang, F. Sun, Y. Zhang, L. Li, H. Chen, Q. Wu and J.C. Yu, *J. Mater. Chem.*, **20**, 5641 (2010);
    https://doi.org/10.1039/b926930d

16. S.H. Baeck, K.S. Choi, T.F. Jaramillo, G.D. Stucky and E.W. McFarland, *Adv. Mater.*, **15**, 1269 (2003);
    https://doi.org/10.1002/adma.200304669

17. C. Wang, C. Shao, X. Zhang and Y. Liu, *Inorg. Chem.*, **48**, 7261 (2009);
    https://doi.org/10.1021/ic9005983

18. W.W. Wang, Y.J. Zhu and L.X. Yang, *Adv. Funct. Mater.*, **17**, 59 (2007);
    https://doi.org/10.1002/adfm.200600431

19. X. Wang, X. Lu, B. Liu, D. Chen, Y. Tong and G. Shen, *Adv. Mater.*, **26**, 4763 (2014);
    https://doi.org/10.1002/adma.201400910

20. L. Sun, X. Wang, K. Zhang, J. Zou and Q. Zhang, *Nano Energy*, **22**, 11 (2016);
    https://doi.org/10.1016/j.nanoen.2015.12.007

21. K.S. Novoselov, A.K. Geim, S.V. Morozov, D. Jiang, Y. Zhang, S.V. Dubonos, I.V. Grigorieva and A.A. Firsov, *Science*, **306**, 666 (2004);
    https://doi.org/10.1126/science.1102896

22. M. Srivastava, J. Singh, T. Kuila, R.K. Layek, N.H. Kim and J.H. Lee, *Nanoscale*, **7**, 4820 (2015);
    https://doi.org/10.1039/C4NR07068B

23. J. Zhu, D. Yang, Z. Yin, Q. Yan and H. Zhang, *Small*, **10**, 3480 (2014);
    https://doi.org/10.1002/smll.201303202

24. K.S. Novoselov, V.I. Fal2ko, L. Colombo, P.R. Gellert, M.G. Schwab and K. Kim, *Nature*, **490**, 192 (2012);
    https://doi.org/10.1038/nature11458

25. F. Bonaccorso, L. Colombo, G. Yu, M. Stoller, V. Tozzini, A.C. Ferrari, R.S. Ruoff and V. Pellegrini, *Science*, **347**, 1246501 (2015);
    https://doi.org/10.1126/science.1246501

26. T.H. Han, Y. Lee, M.R. Choi, S.H. Woo, S.H. Bae, B.H. Hong, J.H. Ahn and T.W. Lee, *Nat. Photonics*, **6**, 105 (2012);
    https://doi.org/10.1038/nphoton.2011.318

27. M. Pumera, *Chem. Rec.*, **9**, 211 (2009);
    https://doi.org/10.1002/tcr.200900008

28. X. Sun, Z. Liu, K. Welsher, J.T. Robinson, A. Goodwin, S. Zaric and H. Dai, *Nano Res.*, **1**, 203 (2008);
    https://doi.org/10.1007/s12274-008-8021-8

29. R. Raccichini, A. Varzi, S. Passerini and B. Scrosati, *Nat. Mater.*, **14**, 271 (2015);
https://doi.org/10.1038/nmat4170

30. Z.S. Wu, G. Zhou, L.C. Yin, W. Ren, F. Li and H.M. Cheng, *Nano Energy*, **1**, 107 (2012);
https://doi.org/10.1016/j.nanoen.2011.11.001

31. S. Bae, H. Kim, Y. Lee, X. Xu, J.-S. Park, Y. Zheng, J. Balakrishnan, T. Lei, H. Ri Kim, Y.I. Song, Y.-J. Kim, K.S. Kim, B. Özyilmaz, J.-H. Ahn, B.H. Hong and S. Iijima, *Nat. Nanotechnol.*, **5**, 574 (2010);
https://doi.org/10.1038/nnano.2010.132

32. M.D. Stoller, S. Park, Y. Zhu, J. An and R.S. Ruoff, *Nano Lett.*, **8**, 3498 (2008);
https://doi.org/10.1021/nl802558y

33. R.S. Edwards and K.S. Coleman, *Nanoscale*, **5**, 38 (2013);
https://doi.org/10.1039/C2NR32629A

34. Y. Zhu, S. Murali, W. Cai, X. Li, J.W. Suk, J.R. Potts and R.S. Ruoff, *Adv. Mater.*, **22**, 3906 (2010);
https://doi.org/10.1002/adma.201001068

35. H.P. Boehm, *Angew. Chem. Int. Ed.*, **49**, 9332 (2010);
https://doi.org/10.1002/anie.201004096

36. C. Soldano, A. Mahmood and E. Dujardin, *Carbon*, **48**, 2127 (2010);
https://doi.org/10.1016/j.carbon.2010.01.058

37. V. Skákalová, V. Vretenár, L. Kopera, P. Kotrusz, C. Mangler, M. Mesko, J.C. Meyer and M. Hulman, *Carbon*, **72**, 224 (2014);
https://doi.org/10.1016/j.carbon.2014.02.006

38. H. Liu, W.R. Cao, Y. Su, Z. Chen and Y. Wang, *J. Colloid Interface Sci.*, **398**, 161 (2013);
https://doi.org/10.1016/j.jcis.2013.02.007

39. B. Murugesan, A. Sivakumar, A. Loganathan and P. Sivakumar, *J. Taiwan Inst. Chem. Eng.*, **71**, 364 (2017);
https://doi.org/10.1016/j.jtice.2016.11.020

40. Y. Xu, H. Bai, G. Lu, C. Li and G. Shi, *J. Am. Chem. Soc.*, **130**, 5856 (2008);
https://doi.org/10.1021/ja800745y

41. A. Wang, S. Shen, Y. Zhao and W. Wu, *J. Colloid Interface Sci.*, **445**, 330 (2015);
https://doi.org/10.1016/j.jcis.2015.01.017

42. R. Zamiri, H.A. Ahangar, A. Kaushal, A. Zakaria, G. Zamiri, D. Tobaldi and J.M.F. Ferreira, *PLoS One*, **10**, 0131851 (2015);
https://doi.org/10.1371/journal.pone.0122989

43. Y.K. Kho, W.Y. Teoh, A. Iwase, L. Madler, A. Kudo and R. Amal, *ACS Appl. Mater. Interfaces*, **3**, 1997 (2011);
https://doi.org/10.1021/am200247y

44. S.I. El-Hout, S.M. El-Sheikh, H.M.A. Hassan, F.A. Harraz, I.A. Ibrahim and E.A. El-Sharkawy, *Appl. Catal. A Gen.*, **503**, 176 (2015);
https://doi.org/10.1016/j.apcata.2015.06.036

45. B. Lobato, V. Vretenár, P. Kotrusz, M. Hulman and T.A. Centeno, *J. Colloid Interface Sci.*, **446**, 203 (2015);
https://doi.org/10.1016/j.jcis.2015.01.037

46. R. Jain, A.S. Poyraz, D.P. Gamliel, J. Valla, S.L. Suib and R. Maric, *Appl. Catal. A Gen.*, **507**, 1 (2015);
https://doi.org/10.1016/j.apcata.2015.09.041

47. Y. Guo, X. Sun, Y. Liu, W. Wang, H. Qiu and J. Gao, *Carbon*, **50**, 2513 (2012);
https://doi.org/10.1016/j.carbon.2012.01.074

48. G. Jnawali, Y. Rao, J.H. Beck, N. Petrone, I. Kymissis, J. Hone and T.F. Heinz, *ACS Nano*, **9**, 7175 (2015);
https://doi.org/10.1021/acsnano.5b01896

49. J. Hu, C. Zou, Y. Su, M. Li, N. Hu, H. Ni, Z. Yang and Y. Zhang, *J. Mater. Chem. C Mater. Opt. Electron. Devices*, **5**, 6862 (2017);
https://doi.org/10.1039/C7TC01208J

50. S. Kaneco, M.A. Rahman, T. Suzuki, H. Katsumata and K. Ohta, *J. Photochem. Photobiol. Chem.*, **163**, 419 (2004);
https://doi.org/10.1016/j.jphotochem.2004.01.012

51. J.J. Vilatela and D. Eder, *ChemSusChem*, **5**, 456 (2012);
https://doi.org/10.1002/cssc.201100536

52. J. Shi, *Chem. Rev.*, **113**, 2139 (2013);
https://doi.org/10.1021/cr3002752

53. M.I. Litter, *Appl. Catal. B*, **23**, 89 (1999);
https://doi.org/10.1016/S0926-3373(99)00069-7

54. S. Alahiane, S. Qourzal, M. El Ouardi, A. Abaamrane and A. Assabbane, *Am. J. Anal. Chem.*, **5**, 445 (2014);
https://doi.org/10.4236/ajac.2014.58053

55. D.F. Ollis, *J. Phys. Chem. B*, **109**, 2439 (2005);
https://doi.org/10.1021/jp040236f

56. A.V. Emeline, V.K. Ryabchuk and N. Serpone, *J. Phys. Chem. B*, **109**, 18515 (2005);
https://doi.org/10.1021/jp0523367

57. J. Matos, J. Laine and J.M. Herrmann, *Appl. Catal. B*, **18**, 281 (1998);
https://doi.org/10.1016/S0926-3373(98)00051-4

58. N.G. Asenjo, R. Santamary'a, C. Blanco, M. Granda, P. A'lvarez and R. Menendez, *Carbon*, **55**, 62 (2013);
https://doi.org/10.1016/j.carbon.2012.12.010

59. A. Gomez-Barea, B. Leckner, A.L. Villanueva Perales and M. Campoy, *Chem. Eng. J.*, **183**, 408 (2012);
https://doi.org/10.1016/j.cej.2011.12.053

60. H. Fu, T. Xu, S. Zhu and Y. Zhu, *Environ. Sci. Technol.*, **42**, 8064 (2008);
https://doi.org/10.1021/es801484x

61. A. Sobczynski, L. Duczmal and W. Zmudzinski, *J. Mol. Catal. Chem.*, **213**, 225 (2004);
https://doi.org/10.1016/j.molcata.2003.12.006

62. E.C. Lima, M.A. Adebayo and F.M. Machado, Carbon Nanomaterials as Adsorbents for Environmental and Biological Applications, Springer, p. 33-69 (2015).

63. M.I. El-Khaiary and G.F. Malash, *Hydrometallurgy*, **105**, 314 (2011);
https://doi.org/10.1016/j.hydromet.2010.11.005

64. J.I. Steinfeld, J.S. Francisco and W.L. Hase, Chemical Kinetics and Dynamics, Prentice Hall Publishing: New Jersey, edn 2 (1999).

65. T. Ahmad, R. Phul, P. Alam, I.H. Lone, M. Shahazad, J. Ahmed, T. Ahamad and S.M. Alshehri, *RSC Adv.*, **7**, 27549 (2017);
https://doi.org/10.1039/C6RA26888A